Journal of Micromechanics and Microengineering

Bio-implantable passive on-chip RF-MEMS strain sensing resonators for orthopaedic applications

To cite this article: Rohat Melik *et al* 2008 *J. Micromech. Microeng.* **18** 115017

View the article online for updates and enhancements.

Related content

- Thermomechanical properties and performance of ceramic resonators for wireless pressure reading at high temperatures
P Sturesson, Z Khaji, S Knaust et al.
- A generalized CMOS-MEMS platform for micromechanical resonators monolithically integrated with circuits
Wen-Chien Chen, Weileun Fang and Sheng-Shian Li
- Topical Review
S Tadigadapa and K Mateti

Recent citations

- Advances in Materials for Recent Low-Profile Implantable Bioelectronics
Yanfei Chen *et al*
- Amos Danielli *et al*
- Split-Ring Resonator-Based Sensors on Flexible Substrates for Glaucoma Monitoring
Gizem Ekinci *et al*

IOP ebooks™

Bringing you innovative digital publishing with leading voices to create your essential collection of books in STEM research.

Start exploring the collection - download the first chapter of every title for free.

This content was downloaded from IP address 139.179.72.98 on 09/12/2018 at 18:30

IOP Publishing | Journal of Micromechanics and Microengineering

J. Micromech. Microeng. **18** (2008) 115017 (9pp) doi:10.1088/0960-1317/18/11/115017

Bio-implantable passive on-chip RF-MEMS strain sensing resonators for orthopaedic applications

Rohat Melik[1], Nihan Kosku Perkgoz[1], Emre Unal[1], Christian Puttlitz[2] and Hilmi Volkan Demir[1]

[1] Department of Electrical and Electronics Engineering, Department of Physics, Nanotechnology Research Center, and Institute of Materials Science and Nanotechnology, Bilkent University, Ankara, 06800, Turkey

[2] Department of Mechanical Engineering, Orthopaedic Bioengineering Research Laboratory, Colorado State University, Fort Collins, CO 80523, USA

Received 1 May 2008, in final form 5 September 2008
Published 7 October 2008
Online at stacks.iop.org/JMM/18/115017

Abstract

One out of ten bone fractures does not heal properly due to improper load distribution and strain profiles during the healing process. To provide implantable tools for the assessment of bone fractures, we have designed novel, bio-implantable, passive, on-chip, RF-MEMS strain sensors that rely on the resonance frequency shift with mechanical deformation. For this purpose, we modeled, fabricated and experimentally characterized two on-chip sensors with high quality factors for *in vivo* implantation. One of the sensors has an area of ∼0.12 mm^2 with a quality factor of ∼60 and the other has an area of ∼0.07 mm^2 with a quality factor of ∼70. To monitor the mechanical deformation by measuring the change in the resonance frequencies with the applied load, we employed a controllable, point load applying experimental setup designed and constructed for *in vitro* characterization. In the case of the sensor with the larger area, when we apply a load of 3920 N, we obtain a frequency shift of ∼330 MHz and a quality factor of ∼76. For the smaller sensor, the frequency shift and the quality factor are increased to 360 MHz and 95, respectively. These data demonstrate that our sensor chips have the capacity to withstand relatively high physiologic loads, and that the concomitant and very large resonant frequency shift with the applied load is achieved while maintaining a high signal quality factor. These experiments demonstrate that these novel sensors have the capacity for producing high sensitivity strain readout, even when the total device area is considerably small. Also, we have demonstrated that our bio-implantable, passive sensors deliver a telemetric, real-time readout of the strain on a chip. Placing two more resonators on the sides of the sensor to serve as transmitter and receiver antennas, we achieved to transfer contactless power and read out loads in the absence of direct wiring to the sensor. With this model, where telemetric measurements become simpler due to the fact that all sensor system is built on the same chip, we obtain a frequency shift of ∼190 MHz with an increase in the quality factor from ∼38 to ∼46 when a load of 3920 N is applied. Therefore, as a first proof of concept, we have demonstrated the feasibility of our on-chip strain sensors for monitoring the mechanical deformation using telemetry-based systems.

(Some figures in this article are in colour only in the electronic version)

1. Introduction

Treatment of complicated bone fractures continues to be a challenge for modern medicine [1]. In fact, approximately 10% of all bone fractures will not heal properly [2]. Most operative treatment schema typically require the implantation of stainless steel or titanium plates. The hardware serves to

 © 2008 IOP Publishing Ltd Printed in the UK

resist high stresses and bear a majority of the load during the early phase of bone tissue healing. As the healing tissue starts to ossify, the load is gradually transferred from the implanted plate to the tissue. Monitoring of the healing process in the acute phase (approximately first 30 days) via radiographic assessment (typically by x-rays) does not have sufficient fidelity to determine if the healing is normal or aberrant. To date, *in vivo*, real-time monitoring of the healing process via monitoring the hardware-to-tissue load transfer has not been possible due to a lack of technological advancement. To address this problem, we hereby introduce a bioimplantable wireless sensor system capable of monitoring the change in loading of an implantable plate in order to determine the quality of the healing process. By using such a remote sensor, it is expected that a continuous healing profile of an individual patient can be recorded during the activities of daily life.

Although biosensors have been studied for a wide range of applications and a good deal of research has been conducted by various groups, there exists limited data with respect to implantable microelectromechanical systems (MEMS) biosensors due to various challenges [3]. One of the drawbacks of current wireless sensors is production of a low quality factor (Q-factor), which can be described as the ratio of the stored to lost energy. To monitor physiological parameters using telemetry-based implantable sensing systems, implantable bio-MEMS based capacitive pressure sensors have only been able to achieve Q-factors of approximately 10 [4, 5]. An important requirement on these sensors is that they maintain a fully on-chip resonator with a high transmission dip at resonance for telemetric sensing applications. Reducing the size of a sensor is another major issue because of the limited space for *in vivo* implantation. In our previous study, we demonstrated the implementation an on-chip resonator operating at 15 GHz with a Q-factor of 93.81 and a small chip size of 195 μm × 195 μm [6]. We effectively utilized a spiral coil geometry and cavity resonator concept, which provided a reduced area and practical implementation with a high Q-factor [6]. In this previous work of our group and the others, we developed RF resonators that were studied and designed from microwave perspective, especially focusing on high-Q performance. These resonators were not previously designed or characterized as MEMS-sensors for mechanical deformation (under applied force), unlike this current work.

In this work for the first, we present a bio-MEMS strain sensor for implantation using a RF-MEMS approach. The operating principle is based on a concomitant resonant frequency shift with mechanical deformation. We aim to sense biological data and transfer it effectively to an antenna outside the body. To interpret the biological data, the input is denoted by the physical load (F), and the output is denoted by the resonant frequency readout (f_0). As the load is applied to the stainless steel plate, it deforms (strains) under the applied stress [7]. Eventually this strain decreases (due to the temporal shift in the load distribution) and modifies the resonant frequency, thus allowing for real-time observation of the healing process in the fracture. Therefore, with the sensor chip we propose and demonstrate, it is possible to measure the change in the strain and hence to assess the healing process by means of this resonance frequency shift. This f_0 shift results from the change in the capacitance of the film between the metal and the substrate because of the modified area with the applied force. Here it is worth noting that the resonator and the capacitive strain sensor are on the same chip in a compact form, which is unique to our design. Previous literature has reported on changes in the capacitance of the chip and resultant resonance frequency shifts [5, 8–10]; however, the area of these devices is relatively large because an additional external capacitor is used to tune the resonator. Also, these previous devices were constrained to very narrow load ranges.

In order to design and fabricate a bio-implantable RF-MEMS sensor based upon resonance frequency shifts, a number of difficult issues need to be addressed. First, human lower extremity loading can be approximately four or five times of its body weight. The implication of this is that a person with a weight of 100 kgf (i.e., 980 N) can apply a load of 500 kgf (i.e., 4900 N) to an implanted stainless steel plate. Therefore, the chip has to withstand relatively high stresses while remaining sufficiently sensitive to indicate the resonance frequency as a function of the applied force. We apply this force to the chip using our experimental setup to have controllable resonance frequency with the applied load. Another constraint to be considered is the device size, since the area of the chip is limited by the plate area (in the range of cm^2). Additionally the materials are required to be biocompatible and not costly. Considering all these constraints, a biocompatible, sensitive, high Q-factor chip with smallest possible area is required to be modeled and produced as the first proof of concept.

2. Theoretical background

To design the sensor circuit, we use a coil structure with spiral geometry for the distributed inductor and capacitor shown in top view and side view in figures 1(*a*) and (*b*), and apply the transmission line theory to model this structure as a resonator. We presented a complete description of our circuit model given in figure 1(*c*), and the characterization of the RF device in our previous studies [6, 11]. In this work, to achieve a high Q-factor, we used the same methodology from microwave perspective as in our previous studies [6, 11]; further details of the RF design can also be found in the literature [12–19]. In this circuit model, C_{film} is the capacitance between the coil and the substrate as in (1), as depicted in figure 1(*b*), and C_S and L_S denote the capacitance between adjacent coils and the inductance of the spiral coil, respectively. R_S and R_{Si} are the resistances of the coil and the substrate, respectively. We use R_P and C_P for the circuit conversions [6, 11] and calculate them as in (2) and (3). Finally combining all these, we find the Q-factor of the inductor (Q_{ind}) as in (4).

$$C_{\mathrm{film}} = \frac{\varepsilon_0 \varepsilon_r \ell w}{t_{\mathrm{film}}} \tag{1}$$

$$R_P = \frac{1}{\omega^2 C_{\mathrm{film}}^2 R_{\mathrm{Si}}} + \frac{R_{\mathrm{Si}}(C_{\mathrm{film}} + C_{\mathrm{Si}})^2}{C_{\mathrm{film}}^2} \tag{2}$$

$$C_P = C_{\mathrm{film}} \frac{1 + \omega^2 (C_{\mathrm{film}} + C_{\mathrm{Si}}) C_{\mathrm{Si}} R_{\mathrm{Si}}^2}{1 + \omega^2 (C_{\mathrm{film}} + C_{\mathrm{Si}})^2 R_{\mathrm{Si}}^2} \tag{3}$$

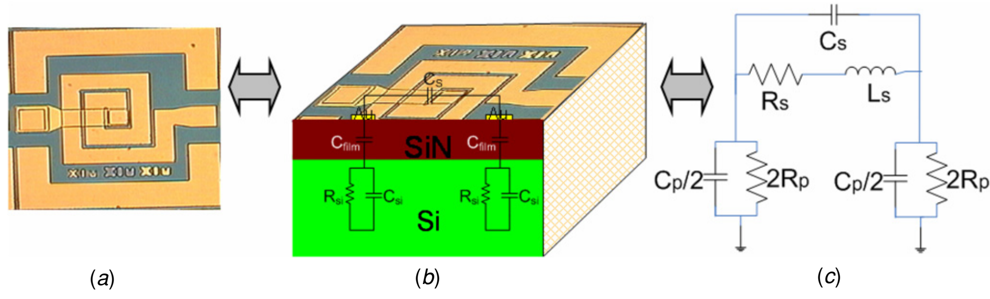

Figure 1. (*a*) The top-view micrograph of a fabricated resonator, (*b*) a side-view schematic of the resonator shown along with the lumped element representations of its physical model and (*c*) our equivalent circuit model of the resonator.

$$Q_{\mathrm{ind}} = \frac{\omega L_S}{R_S} \times \frac{2R_P}{2R_P + \left[\left(\frac{\omega L_S}{R_S}\right)^2 + 1\right] R_S} \times \left[1 - \frac{R_S^2\left(\frac{C_P}{2} + C_S\right)}{L_S} - \omega^2 L_S \left(\frac{C_P}{2} + C_S\right)\right]. \quad (4)$$

To determine the change in the resonant frequency readout we start from the force (F) and stress (σ) relationship. When a force is applied to the structure, it creates stress as given in (5), where A denotes the cross-sectional area of the plate. The stress causes strain (ε) in the structure as in (6), where the strain is calculated from the relationship in (7). E and l represent the Young's modulus (Pa) and length of the plate, respectively. The strain changes the sensor behavior mainly as a result of the modification in the capacitance. As a result we observe a change in the resonance frequency. We apply a point load to our structure to mechanically deform the active device area with the applied load. As we already know the parameters of the deflection, we determine our controllable load from (8) [20]. Here x, y and L represent the positions along beam length, the deflection and the beam length (m), respectively. I is the moment of inertia (m^4).

$$\sigma = \frac{F}{A} \quad (5)$$

$$\sigma = E\varepsilon \quad (6)$$

$$\varepsilon = \frac{\Delta l}{l} \quad (7)$$

$$y(x) = \frac{F}{6EI}(3x^2L - x^3). \quad (8)$$

3. Sensor design and fabrication

With the aim of designing a biocompatible, high Q-factor sensor resonator chip with a small size and high frequency shift, we first need to determine the circuit that measures the change in the resonance frequency to operate either in a passive or active mode. In the case of an active circuit, minimization of the circuit space is restricted by the power supply and the device size becomes larger with a limited deformation of the device. Therefore, we prefer to use a passive circuit. Although using GaAs as the substrate material would enhance the Q-factor, we use Si for its better biocompatibility characteristics. Nonconductive Si hinders the parallel plate capacitance and the proper operation of the resonator. On the other hand, conductive Si decreases the Q-factor. Therefore, we employ a highly resistive Si substrate.

The selection of the dielectric layer affects the capacitance and the Q-factor. Si_3N_4 has a relatively high dielectric constant (as high as 8) and low loss, and also it is biocompatible. There are some dielectric materials that feature lower Young's moduli than Si_3N_4; however, they have higher loss and lower dielectric constants, resulting in a low Q-factor and the change of resonance frequency would not be as high as that of Si_3N_4. As a result, considering the trade-off between high Q-factor, small dimensions and high shift of resonance frequency, we select Si_3N_4 as the dielectric layer.

To observe the change in the resonance frequency (Δf_0) easily, we need to have a sufficiently low Young's modulus of the dielectric material as given in (6) since the stress is set to a fixed value and Young's moduli of Si and metal are already high. Therefore, when the area of the dielectric layer is changed, the capacitance is modified as in (1) and we realize a shift in the resonance frequency, which also affects the Q-factor as in (4). In the case of metals, their Young's moduli are nearly the same, which means that the choice of the metal is trivial for the shift of resonance frequency. Although Al and Cu are mostly utilized as metal layers, they are not biocompatible. Therefore, for future *in vivo* applications in mind, we prefer to use Au as the metal layer.

When deciding on the film thickness, once again we are required to consider the critical constraints such as a high Q-factor and small allowable dimension. Thus, our approach is to favor the high capacitance, which can be obtained from the tank circuit capacitance [6, 11] as opposed to considering this element as a parasitic capacitance (as it has been previously typically treated by other research groups). Hence, we choose a film thickness (t_{film}) as low as 0.1 μm. Using the film capacitance for self-tuning the resonator will also increase the resonance frequency shift and improve the sensor sensitivity compared to the approach of using an external capacitor for tuning.

To realize a high-performance sensor, the width of the metal is a critical design issue because an increase in the width would also increase the Q-factor and the resonance frequency, but this would produce an associated increase in the area at the same time. Therefore, considering these constraints, we choose an optimal value for the width. Also the metal

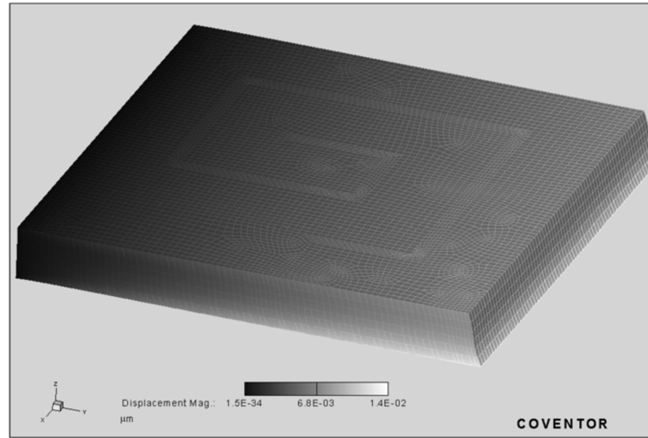

Figure 2. Illustration of the deformed device when a load of 1960 N is applied from the bottom. The area and the thickness of the device are fixed to 340 μm × 340 μm and 500 μm, respectively. The z-direction is scaled down by a factor of 10 for a better view of the image.

spacing affects the device performance. A lower spacing increases resonance frequency and leads to a more compact chip. However, an increased width and decreased spacing lead to parasitic effects which would decrease the Q-factor. So the value of the spacing should be carefully adjusted. With our design methodology, we find that we do not need to consider the effect of the skin depth, as this effect is relatively reduced and high Q-factors are still obtained; the derivation of this conclusion can be found elsewhere [11].

Increasing the number of turns of the coil decreases the Q-factor and the resonance frequency and increases the area of the chip. Two turns is the minimum number needed to produce a full coil and this is the geometry used in our design. Decreasing the total area leads to an improved Q-factor and a higher resonance frequency. Also, a smaller inner diameter increases the Q-factor and resonance frequency. However, decreasing the inner diameter to a point where it is less than the spacing causes additional parasitic effects. Therefore, considering the width, the spacing, the inner diameter and the number of turns, we choose an optimal area. R_p, which was given in (2), represents the combined resistance of our coil model and is an effective component to determine the substrate losses. We choose a high-resistivity substrate to get a high R_{Si} and thus a high R_P. Therefore, in our model, the substrate loss factor is nearly independent of the frequency, and also, we obtain a high Q-factor. C_p, corresponding to the capacitive component of the combined impedance and calculated as in (3), has a significant effect on the self-resonance factor. Lower C_p results in an enhanced resonance frequency.

Taking all these different factors into account, we designed two sensor chips with the parameters determined as shown in table 1. Here L_C and W_C represent total length and total width of the device, respectively. N is the number of turns, w is the width of each coil, and s is the spacing between coils. Also t_{film} and t_{metal} represent the thickness of the dielectric film and the thickness of the metal, respectively.

Based on the parameters of sensor-1, we ran a simulation using a commercially-available finite element software package (Coventorware) to monitor the strain induced in the device when a load of 1960 N is applied. Figure 2 shows the resulting displacement field. From the simulation, we observe that the area of the dielectric film changes, modifying the value of C_{film}. We note that the change in the area is not uniform, which results in a nonlinear change in C_{film}, and thus, in the resonance frequency, as a function of the applied load (where the resonance frequency is calculated from the point that Q_{ind} becomes zero as in (4)).

We numerically calculated the inductance of the spiral coil (L_s), which is obtained by the addition of self-inductance with the positive mutual inductance and subtracted by the negative mutual inductance. We observe a very good agreement with the results obtained by the MemHenry suite of Coventorware (table 2).

We fabricate our sensors using standard MEMS fabrication processes. For fabrication, the substrate is initially patterned with lithography and metallization is performed to obtain a thickness of 0.1 μm using Au. Then the structure is coated by a 0.1 μm thick Si_3N_4 layer using PECVD. Patterning is realized with lithography and holes are opened using wet etching by HF. The open parts are metallized with the boxcoater at a thickness of 0.1 μm (Au). Finally, the shape of the device is given by a third lithography step and the process is completed with a 0.1 μm thick Au metallization. The fabricated device is presented in the inset of figure 3(a).

Table 1. Our device parameters.

	L_c (μm)	W_c (μm)	N	w (μm)	s (μm)	t_{film} (μm)	t_{metal} (μm)
Sensor-1	340	340	2	60	10	0.1	0.1
Sensor-2	270	270	2	50	5	0.1	0.1

Table 2. The theoretical and numerical L_S values for sensor-1 and sensor-2.

	Theoretical L_S (nH)	Numerical L_S (nH)
Sensor-1	2.854	2.842
Sensor-2	2.260	2.244

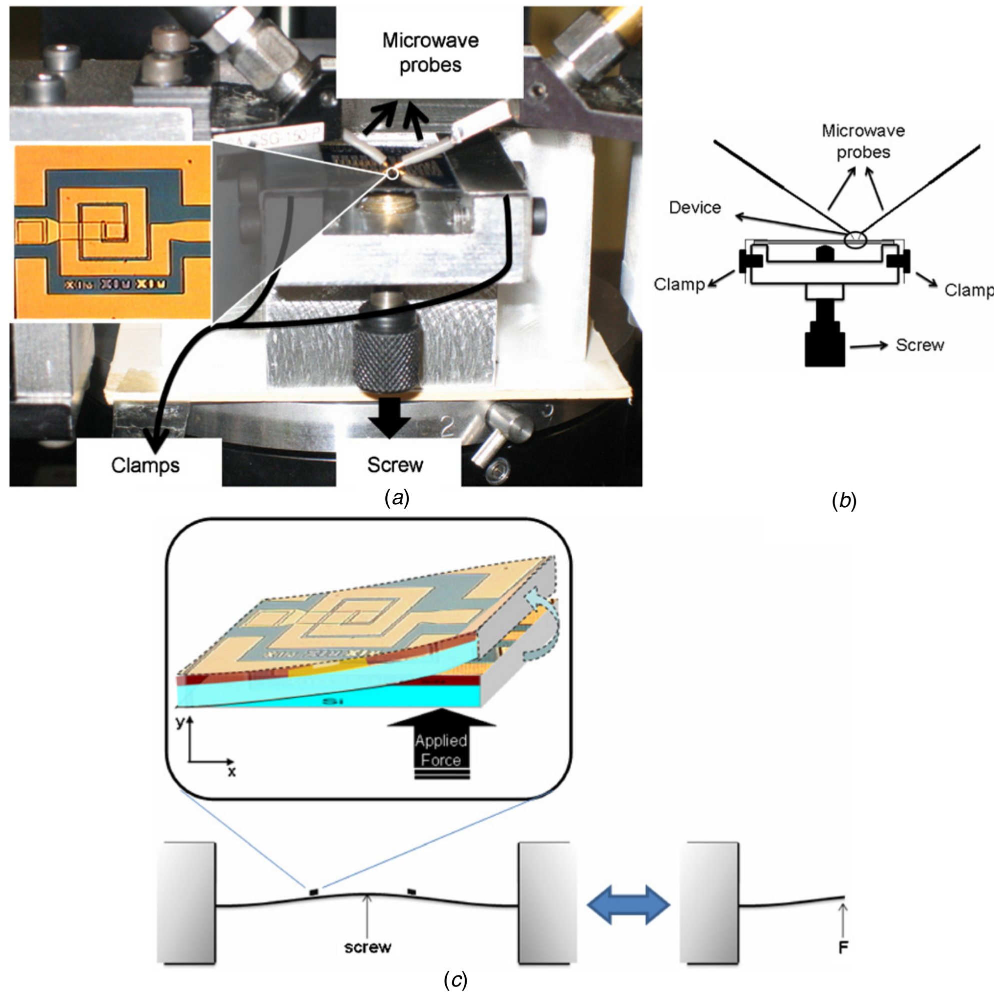

Figure 3. (*a*) The experimental setup along with the fabricated sensor in the inset, (*b*) the cross-sectional sketch of our experimental setup and its components and (*c*) illustration of the mechanical deformation when the force is applied.

4. Experimental characterization

The experimental characterization consists of applying a point load in a controlled manner (figure 3). We use two thin clamps at the edges to fix the silicon substrate as shown in figures 3(*a*) and (*b*). There is a hole in the middle and we placed the silicon substrate into this aperture, fixing the substrate to the edges of the experimental apparatus sketched in figure 3(*b*). We used the screw below the silicon substrate to control and modify the load in a controllable manner. We used an ultra fine adjustable screw so that we could easily modify the applied load. The tip of the screw is a critical part as it should not penetrate or cause failures in the silicon substrate when applying high loads. After fixing our substrate, we measure S_{21} parameters of our device with microwave probes as presented in figures 3(*a*) and (*b*). When we apply load to the whole chip by using screw, a point load is applied to our device while it deforms on the chip as shown in figure 3(*c*).

In figures 4(*a*) and (*b*), S_{21} parameters (in dB) are given as a function of the frequency for sensor-1 and sensor-2, respectively. In figures 4(*c*) and (*d*) magnified views of the resonance regions are shown for sensor-1 and sensor-2, respectively. One can clearly see the differences between the sensor responses without any deformation (no load) and then also with deformation. In the case of no deformation for sensor-1, the resonance frequency was measured to be 11.48 GHz, also given in table 3, with a *Q*-factor of 59.98. When we apply 1960 N, the resonance frequency changes to 11.72 GHz, indicating a 240 MHz shift (also summarized in table 4). When we apply a load of 2940 N, the resonance frequency increases to 11.78 GHz and for 3920 N, it becomes 11.81 GHz (table 3). Therefore, for a load of 2940 N, we obtain a shift of 2940 MHz and for 3920 N, a shift of 330 MHz in the resonance frequency as compared to the initial condition (table 4). Also, the *Q*-factor of the sensor changes from 59.98 to 70.35 when 1960 N load is applied. For a load of 2940 N, the *Q*-factor is 74.32 and for 3920 N, the *Q*-factor is 76.00 (table 5).

Table 3. The resonance frequencies of the sensors with the changing load values.

Load	No load	1960 N	2940 N	3920 N
Sensor-1	11.48 GHz	11.72 GHz	11.78 GHz	11.81 GHz
Sensor-2	13.59 GHz	13.84 GHz	13.91 GHz	13.95 GHz

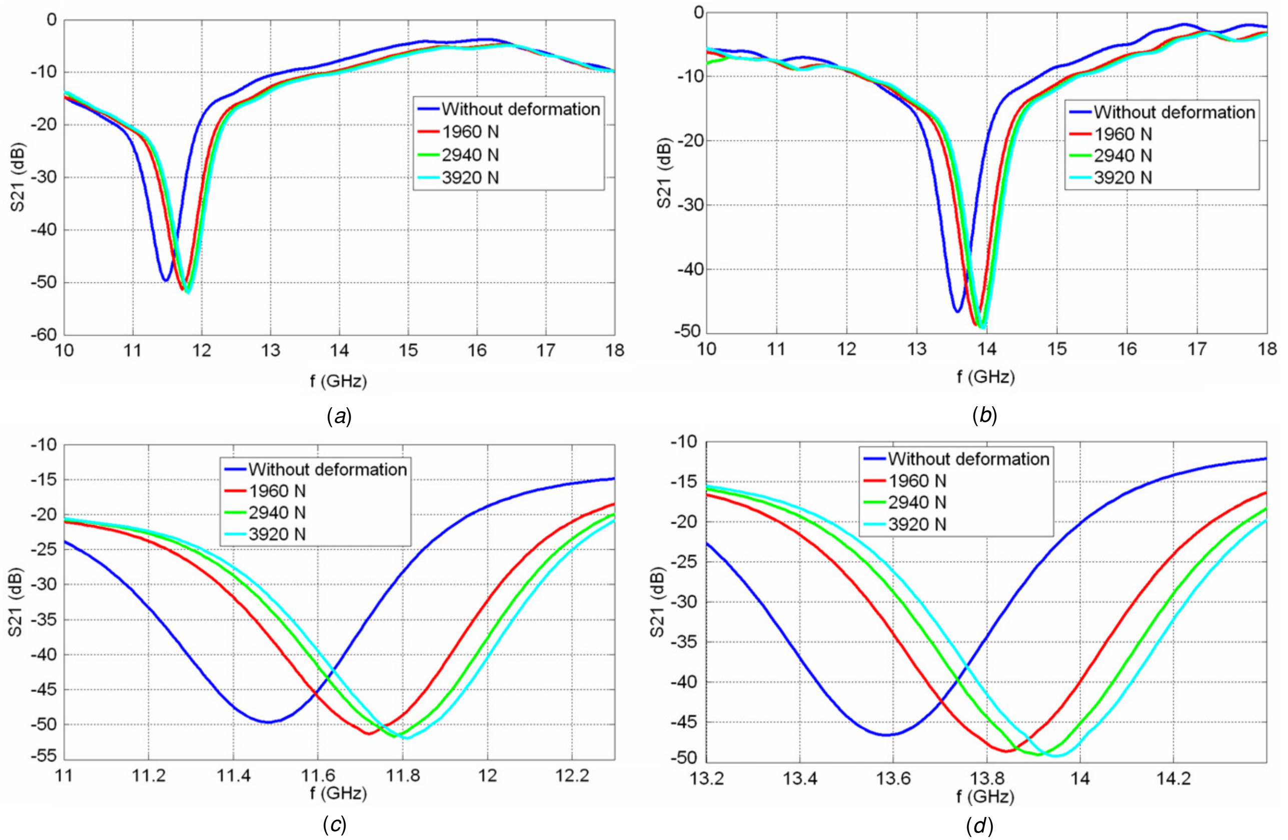

Figure 4. Experimental measurements of S_{21} parameters as a function of frequency for (*a*) sensor-1 and (*b*) sensor-2, along with their zoom-in resonance regions for (*c*) sensor-1 and (*d*) sensor-2, respectively, for the cases without deformation and when loads of 1960 N, 2940 N and 3920 N are applied.

Table 4. The shift of resonance frequencies of the sensors with the changing load values.

Load	1960 N	2940 N	3920 N
Sensor-1	240 MHz	300 MHz	330 MHz
Sensor-2	250 MHz	320 MHz	360 MHz

Table 5. *Q*-factors with the changing load values.

Load	No load	1960 N	2940 N	3920 N
Sensor-1	59.98	70.35	74.32	76.00
Sensor-2	69.91	87.87	89.22	95.39

Figure 4(*b*) shows S_{21} parameter of sensor-2 in decibels as a function of the frequency. Similar to sensor-1, the resonance frequency increases with the applied load. For the no-deformation case, the resonance frequency is 13.59 GHz (table 3) and the *Q*-factor is 69.91 (table 5). After the application of 3920 N load, the resonance frequency becomes 13.95 GHz, representing a resonance frequency shift of 360 MHz (table 4) with a *Q*-factor of 95.39. For 1960 N a 13.84 GHz resonance frequency was measured (table 3) with an 87.87 *Q*-factor (table 5).

From these experimental results it is clear that the resonance frequency increases with the applied load. This can be explained theoretically by the decrease in the area, and hence the resulting decrease in the capacitance (figure 2), leading to an increase in the resonance frequency with the applied load. We also observe that the shift is not linear with respect to the applied load and thus the induced strain (which is experimentally obtained in the reference strain measurements using high-quality semiconductor based wired strain gauges, made by Kyowa, Japan, with a gauge factor of 178) (figure 5). The decrease in the area of the capacitance is not linear so the change in the capacitance is not linear and also capacitance affects the resonance frequency nonlinearly as in (4), and, accordingly, our observation that the change in the resonance frequency is nonlinear with the applied load is congruent with our theoretical derivation.

We can consider the shift of resonance frequency from other perspectives. For example, we can define sensitivity with respect to the applied force as $\frac{\Delta f_0}{F}$. Since we have similar geometries in sensor-1 and sensor-2, which are both rectangular, and they are fabricated with the same fabrication procedure, they are expected to have nearly the same level of sensitivity. For sensor-1 we have 330 MHz resonance frequency shift with 3920 N of applied load. So we have 0.0842 MHz N^{-1} sensitivity. For sensor-2 we have 360 MHz resonance frequency shift with 3920 N of applied load, and hence, 0.0918 MHz N^{-1} sensitivity. The sensor with a higher f_0 will have a higher sensitivity since a higher frequency means a slightly higher shift. Also, we can define sensitivity with respect to the induced strain as $\frac{\Delta f_0}{\varepsilon}$. Because of the structure

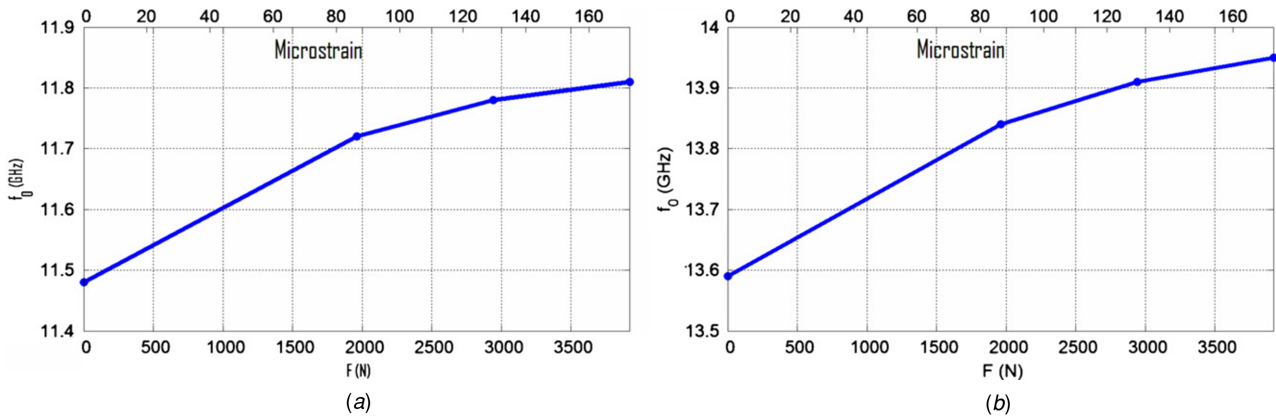

Figure 5. Resonance frequency (f_0) as a function of the externally applied load and the induced strain (microstrain) (*a*) for sensor-1 and (*b*) for sensor-2.

of our load setup, which is explained in detail and illustrated in figure 2, the minimum strain that we can reproducibly apply is 81.5 microstrain, while the maximum strain that we can controllably apply is 172.8 microstrain. For sensor-1 we have 330 MHz resonance frequency shift with an induced strain of 172.8 microstrain while we have 360 MHz resonance frequency shift with 172.8 microstrain for sensor-2. So for sensor-1, we have 1.9 MHz/microstrain sensitivity while we have 2.1 MHz/microstrain sensitivity for sensor-2. Similar to the sensitivity defined with respect to the applied load, the sensor with higher f_0 expectedly yields a slightly higher sensitivity also with respect to strain. For another comparison, we can use another definition: relative shift, which is $\frac{\Delta f_0}{f_0}$ at a given applied load. For sensor-1, under 3920 N, we have a shift of 330 MHz at 11.48 GHz resonance frequency; thus we have a relative shift of 2.88%. For sensor-2 we have 360 MHz shift at 13.59 GHz resonance frequency; thus we have a relative shift of 2.65%. From these results, we observe that we have nearly the same sensitivities and relative shifts. Also, theoretically we consider that if two sensors exhibit the same relative shift, the sensor that has a higher resonance frequency will have a higher change of resonance frequency, and hence a higher sensitivity. Experimentally, we find out that although sensor-2 has a slightly lower relative shift compared to sensor-1, sensor-2 has a slightly higher sensitivity. Presently, by exploring different geometries, different fabrication procedures and different operating frequencies, we are working on increasing the sensitivity and relative shift.

Another important conclusion of our experiments is that the Q-factor of the device is different for each applied load and the resulting strain, as was predicted theoretically. The increase is shown in figure 6. When L_C decreases, the resonance frequency and the Q-factor are increased while the area decreases, as calculated in (4). Therefore, it is expected that sensor-2 has a higher resonance frequency and Q-factor compared to sensor-1. When the capacitance is decreased, the Q-factor is improved as calculated from (4). Therefore, experimentally we observe an increase both in the resonance frequency and the Q-factor as shown in figure 6. Also, since the capacitance change is not linear with applied load and change of the capacitance affects the Q-factor nonlinearly from (4),

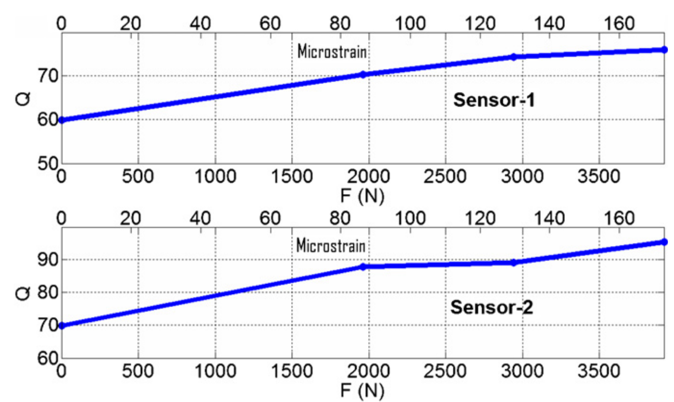

Figure 6. Q-factor as a function of the applied load and the induced strain (microstrain) for sensor-1 (top) and for sensor-2 (bottom).

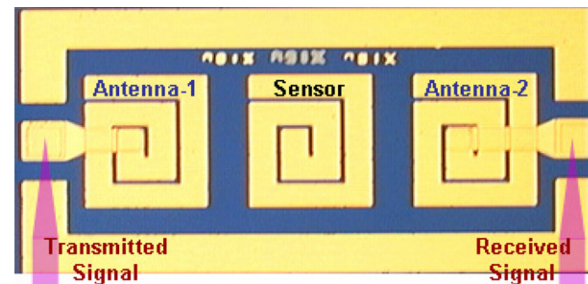

Figure 7. A plan-view micrograph of our fabricated 270 μm × 270 μm on-chip sensor along with the on-chip antennas for communication.

the Q-factor change is theoretically expected to be nonlinear with the applied load. From table 5, we also experimentally observe that the increase in the Q-factor with applied load is not fully linear.

There is a strong demand for implantable chips that measure the change in hardware stress without any external wiring. This would allow the treating clinician to remotely measure and report the information. Therefore, to verify the wireless performance of our sensor, we utilized a telemetry-based implantable sensing system to monitor the resonant frequency shift as a function of the physical load (figure 7). This system consists of two antennas on the chip to serve as

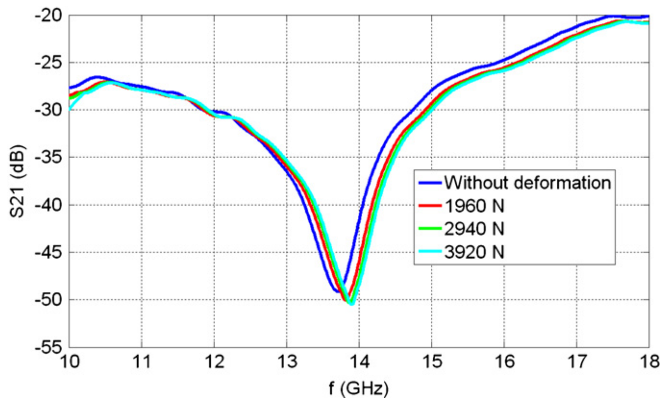

Figure 8. Experimental measurement of S_{21} parameters for the sensor under different loads taken by using the transmitter and receiver antennas.

external antennas. Between these antennas there is the device under test used as the sensor. The telemetric sensor and the antennas have the same dimensions as those of sensor-2.

Similar to the previous cases, we detected strain by measuring the resonance frequencies of the system without any applied load and after applying different loads to the sensor chip. By using three similar resonators, we set up a telemetric system on the same chip. The S_{21} parameter is plotted as a function of the frequency in figure 8. Just like the previous cases, the area of the chip decreases and the resonance frequency increases with the applied load. Without deformation, the resonance frequency and the Q-factor were found to be 13.71 GHz and 38, respectively. After applying a 3920 N, the resonance frequency and the Q-factor was measured to be 13.9 GHz and 46, respectively, representing a resonance frequency shift of 190 MHz.

5. Conclusions

We designed, fabricated and experimentally characterized a high Q-factor, bio-implantable RF-MEMS strain sensor to monitor the fracture healing process by measuring the change in the strain. Such a sensor of our design can withstand loads up to 3920 N without deterioration in the Q-factor, even for chip areas smaller than 0.1 mm^2. When a load of 3920 N is applied to the sensor with an area of 340 μm $\times$ 340 μm (sensor-1), the resonance frequency is shifted by 330 MHz and the Q-factor is increased from ~60 to ~76. As the area is decreased to 270 μm $\times$ 270 μm (sensor-2), we observe that the resonance frequency shift becomes 360 MHz and the Q-factor is increased from ~70 to ~95. We both theoretically and experimentally showed that our sensors can be utilized for assessing the osseous fractures through monitoring the shift in the resonance frequency. We also showed that our approach can be modified to work telemetrically. By fabricating three devices, one sensor and two antennas on the same chip, to set up a telemetric system, we demonstrated that the wireless measurement of the resonant frequency shift is possible. In this case, the resonance frequency and the Q-factor are increased when a load is applied. As a result of this pilot study, we believe that, by observing the change in resonance frequency, surgeons can evaluate the fracture healing process longitudinally. This paper is the first theoretical and experimental proof of this concept. For human implantation applications, the resonance frequency needs to be shifted to a lower range where absorption becomes less considerable. Our future research directions will include improving our sensor to operate within the constraints of the implantation applications.

Acknowledgment

This work is supported by the European Science Foundation (ESF) European Young Investigator Award (EURYI) and the Turkish National Academy of Sciences (TÜBA) Distinguished Young Scientist Award (GEBIP), and TÜBITAK EEEAG 105E066, 105E065, 104E114, 106E020, 107E088 and 107E297, and EU IRG MOON 021391. We are pleased to acknowledge M Yorulmaz for his assistance in using Coventorware, Dr A Dana and E Karaman for their help in the construction of our experimental setup, and Dr Z Dilli for fruitful discussions with her.

References

[1] Schuylenbergh K V, Puers R, Rodes F, Burny F, Donkenvolcke M and Moulart F 1992 Monitoring orthopaedic implants using active telemetry *Proc. Ann. Int. Conf. IEEE* **6** 2672–3
[2] Einhorn T A 1995 Enhancement of fracture healing *J. Bone Joint Surg.* **77** 940–56
[3] Grayson A C R, Shawgo R S, Johnson A M, Flynn N T, Li Y, Cima M J and Langer R A 2004 BioMEMS review: MEMS technology for physiologically integrated devices *Proc. IEEE* **92** 6–21
[4] Simons R N and Miranda F A 2005 Radiation characteristics of miniature silicon square spiral chip antenna for implantable bio-MEMS sensors *Antennas and Propagation Soc. Int. Symp., IEEE* vol 1B pp 836–9
[5] Simons R N, Hall D G and Miranda F A 2004 RF Telemetry system for an implantable Bio-MEMS sensor *IEEE MTT-S Inter. Microwave Symp. Digest* vol 3 pp 1433–6
[6] Melik R, Perkgoz N K, Unal E, Dilli Z and Demir H V 2008 Design and realization of a fully on-chip high-Q resonator at 15 GHz on silicon *IEEE Trans. Electron Dev.* in press
[7] Stoffel K, Klaue K and Perren S M 2000 Functional load of plates in fracture fixation *in vivo* and its correlate in bone healing *Injury* **31** 37–50
[8] Simons R N, Hall D G and Miranda F A 2004 Spiral chip implantable radiator and printed loop external receptor for RF telemetry in bio-sensor systems *Radio and Wireless Conf., IEEE* pp 203–6
[9] Miranda F A, Simons R N and Hall D G 2004 Validation of radio frequency telemetry concept in the presence of biological tissue-like stratified media *IEEE Antennas and Propagation Society Inter. Symp. Digest* vol 2 pp 1335–8
[10] Simons R N and Miranda F A 2003 Radio frequency telemetry system for sensors and actuators *US Patent* 6667725
[11] Melik R and Demir H V 2008 Implementation of high quality-factor on-chip tuned microwave resonators at 7 GHz *Microw. Opt. Technol. Lett.* in press
[12] Yue C P and Wong S S 1998 On-chip spiral inductors with patterned ground shields for Si-based RF IC's *IEEE J. Solid-State Circuits* **33** 743–52
[13] Bahl I 2003 *Lumped Elements for RF and Microwave Circuits* (London: Artech House)

[14] Collin R E 1992 *Foundations for Microwave Engineering* (New York: McGraw Hill)
[15] Pozar D M 2005 *Microwave Engineering* (New York: Wiley)
[16] Greenhouse H M 1974 Design of planar rectangular microelectronic inductors *IEEE Trans. Parts Hybrids Packag.* **10** 101–9
[17] Lee T H 1998 *The Design of CMOS Radio-Frequency Integrated Circuits* (New York: Cambridge University Press)
[18] Yue C P, Ryu C, Lau J, Lee T H and Wong S S 1996 A physical model for planar spiral inductors on silicon *IEEE Int. Electron Dev. Meeting* pp 155–8
[19] Koutsoyannopoulos Y K and Papananos Y 2000 Systematic analytic and modeling of integrated inductors and transformers in RFIC design *IEEE Trans. Circuits Syst.* **47** 699–713
[20] Senturia S D 2001 *Microsystem Design* (Kluwer: Academic)